communications materials

A Nature Portfolio journal

Article

https://doi.org/10.1038/s43246-025-00786-3

Synthesis of tubular MXenes with carbon fiber template and use as anodes in lithium-ion batteries

Check for updates

Filipa M. Oliveira [1] ✉, Bing Wu[1], Vlastimil Mazánek[1], Vojtěch Kundrát[2,3], Kristýna Bukvišová[2,4], Lothar Houben[5], Zdeněk Sofer [1] ✉ & Jesus Gonzalez-Julian [6] ✉

Shaping the morphology of 2D materials is essential for tuning their properties. This is especially true for MXenes, a class of 2D materials, as fine morphological control is the key to unlocking their potential. Here, $Ti_3C_2T_x$ MXene is synthesized using carbon fibers as both the carbon source and template, creating a unique tubular morphology where the MXene layers align along the tube. The tubular $Ti_3C_2T_x$ MXene and corresponding precursor MAX phase are synthesized by molten salts shielded synthesis method in air. Comprehensive characterization confirms that the MXene retains the tubular structure conferred by the carbon fiber. Preliminary electrochemical measurements as an anode material in lithium-ion batteries show an initial discharge capacity and good rate performance at a high current density, indicating potential for high-power applications. Furthermore, this tubular morphology opens new possibilities for MXenes in gas sensing, liquid filtration processes, and other applications that require fast diffusion.

MXenes, a unique class of two-dimensional (2D) transition metal nitrides and carbides, have rapidly attracted significant interest since the discovery of the first MXene ($Ti_3C_2T_x$) in 2011[1]. The precursor materials, known as MAX phases, are layered transition metal compounds with the general formula $M_{n+1}AX_n$, where "M" represents a transition metal, "A" is an element (typically aluminum or silicon), and "X" is carbon and/or nitrogen. The variable n (ranging from 1 to 4) specifies the number of M-layers separating the A-layers[2,3]. MAX phases are known for their remarkable combination of properties, including high electrical and thermal conductivity, excellent machinability, thermal shock resistance, and damage tolerance, along with the inherent benefits of ceramics, such as high Young's modulus, oxidation resistance, lightweight, and stability at elevated temperatures[4]. The MXenes results from the selective etching of "A" element in the precursor MAX phase[1], so the chemical formula $M_{n+1}X_nT_x$, where T_x stands for surface termination groups such as -Cl, -F, -O, or -OH[5]. This selective etching results in a 2D material with electrically conductive properties, a large surface area, and hydrophilicity, making MXenes suitable for a wide range of applications such as energy conversion and storage[6], catalysis[7], electromagnetic interference shielding[8], and sensors[7,9].

The quality and performance of MXenes are intrinsically linked to the properties of the precursor MAX phase, emphasizing the importance of optimizing MAX phase synthesis. The synthesis of MAX phases typically requires high temperatures and, in some cases, high pressures, which can limit the control over particle size and morphology. Molten salt (MS) synthesis has emerged as a versatile method to address these challenges, providing a medium for enhanced ion diffusion and reaction kinetics, reducing the synthesis temperature[4]. The carbon source is another critical factor that influences the synthesis and characteristics of the MAX phases. It serves as a template during synthesis, significantly affecting the features of MAX phase powders and the resulting MXenes.

Traditionally, graphite has been used as the carbon source in synthesizing carbide-MAX phases due to its availability and low price[4], typically producing micrometer-sized particles. However, the potential for alternative carbon sources with different shapes, sizes, and morphologies remains underexplored. Investigating these alternatives could allow finer morphological control and properties inherent to the selected carbon allotrope. Recent research has addressed this by using alternative carbon precursors to prepare MAX phases with distinct morphologies, such as

[1]Department of Inorganic Chemistry, Faculty of Chemical Technology, University of Chemistry and Technology Prague, Technická 5, 166 28 Prague 6, Czech Republic. [2]Thermo Fisher Scientific, Vlastimila Pecha 12, 627 00 Brno, Czech Republic. [3]Department of Molecular Chemistry and Materials Science, Weizmann Institute of Science, Herzl St 234, 7610001 Rehovot, Israel. [4]Central European Institute of Technology, Brno University of Technology, Purkyňova 123, 612 00 Brno, Czech Republic. [5]Department of Chemical Research Support, Weizmann Institute of Science, Herzl St 234, 7610001 Rehovot, Israel. [6]Chair of Ceramics, Institute of Mineral Engineering (GHI), RWTH Aachen University, Forckenbeckstrasse 33, 52074 Aachen, Germany. ✉e-mail: filipa.oliveira@vscht.cz; zdenek.sofer@vscht.cz; gonzalez@lcts.u-bordeaux.fr

nanosized Ti_3AlC_2 powders using acetylene black as the carbon precursor in molten salts under argon (Ar), with the corresponding MXene obtained in hydrofluoric acid solution[10]. Hollow Ti_3AlC_2 microrods were also synthesized in NaCl–KCl molten salts in Ar[11]. In the work by Gogotsi and Simon[12], single-walled carbon nanotubes and graphene aerogel as carbon precursors allowed the synthesis of nanostructured Ti_2AlC and Ti_3AlC_2 MAX phases, respectively, in NaCl–KCl molten salts, all under an atmosphere of Ar. In the same study, the corresponding MXenes were also obtained in MS, specifically $CuCl_2$ and eutectic LiCl–KCl, under an atmosphere of Ar. The shape and size of the precursor MAX phase directly influenced the diffusion paths and surface area of the resulting MXenes, which are crucial for energy storage applications. These nanosized precursors enabled shorter ion diffusion paths during etching. They enhanced the performance of the MXenes in electrochemical lithium-ion storage applications, highlighting the critical relationship between the morphology of the precursor and the functional properties of the resulting MXenes. Beyond Ti-Al-C MAX phases, Cr_2GaC MAX phases with distinct shapes, including thick films, dense microspheres, and hollow microspheres, were also synthesized using biopolymer-derived carbon sources in a sol-gel-assisted synthesis[13]. All these studies further confirm that the carbon precursor significantly influences the morphology of the synthesized MAX phases, serving as a template for the growth mechanism.

Given the promising potential of alternative carbon sources, we extend this approach by exploring using micro-sized carbon fibers (CF) as both a carbon source and template in synthesizing the Ti_3AlC_2 MAX phase to achieve an MXene with a tubular structure. It is well-known that CF offer several advantages, including high stiffness, strength, and corrosion resistance, enhancing the properties of the resulting synthesized compounds. We employ the molten salt shielded synthesis (MS^3) method in air[14], with KBr as the reaction medium for the synthesis of the MAX phase and $CuCl_2$ as a Lewis acid etchant for the preparation of MXene[15,16], where the reaction medium is a shield to prevent the oxidation of the MAX phase and MXene. In particular, the entire process is carried out in the air without using protective atmospheres such as Ar, simplifying the procedure, making it accessible to any research laboratory equipped with only a furnace, and significantly reducing costs. This allows for the potential reduction of the environmental impact compared to traditional methods.

Our results demonstrate that CF as a carbon source allows synthesizing a rod-like hollow Ti_3AlC_2 MAX phase, with the corresponding MXene retaining this unique tubular structure. This achievement in the synthesis of MXenes was confirmed by comprehensive morphological and structural characterizations using X-ray diffraction (XRD), X-ray photoelectron spectroscopy (XPS), scanning electron microscopy (SEM), and transmission electron microscopy (TEM). Preliminary electrochemical testing further indicates that this tubular MXene exhibits promising potential as an anode material for lithium-ion batteries, highlighting its structural advantages for applications requiring high surface area and efficient ion transport.

Results and discussion

Synthesis of Ti_3AlC_2 MAX phase

The Ti_3AlC_2 MAX phase was synthesized using the molten salt shielded synthesis (MS^3) method, as detailed in the Experimental section, with carbon fibers (CF) as the carbon source. The microstructure of the CF is shown in Supplementary Fig. 1, clearly observing short CF powders with a homogeneous rod-like morphology.

The synthesis of the Ti_3AlC_2 MAX phase using CF as a carbon source was systematically investigated and optimized by varying the molar ratios of Al and C and the dwell time. This variation was necessary because Al has a low melting point of 660 °C, leading to partial evaporation at elevated temperatures, which requires adding up to 20% excess to compensate[4]. Additionally, carbon often does not fully react to form Ti_3AlC_2, resulting in secondary phases like titanium carbide (TiC), so the carbon content is typically reduced to a nonstoichiometric ratio to minimize this[17]. These factors are well-known when using graphite, a typical carbon source for synthesizing Ti_3AlC_2. However, given the different morphology and structure of microsized CF compared to graphite, it is essential to understand how CF affects the formation of expected microsized Ti_3AlC_2 rods. Therefore, four different ratios were investigated: $Ti_3Al_{1.1}C_{1.8}$, $Ti_3Al_{1.2}C_{1.8}$, $Ti_3Al_{1.1}C_{1.9}$, and $Ti_3Al_{1.2}C_{1.9}$. Supplementary Table 1 summarizes the various conditions set for the syntheses. Syntheses were performed at 1250 °C with a dwell time of 7 h.

Supplementary Fig. 2 shows X-ray diffraction (XRD) patterns of synthesized MAX phases under different stoichiometries, and Supplementary Fig. 3 presents SEM micrographs that provide a detailed view of the morphological evolution of these phases.

For $Ti_3Al_{1.1}C_{1.8}$, the SEM images (Supplementary Figs. 3a, b) show a mixture of typical layered MAX phases and poorly defined microsized tubular structures. The compound appears heterogeneous, indicating an uneven formation of tubular-like structures. The XRD pattern (Supplementary Fig. 2) shows diffractions for Ti_3AlC_2 corresponding to planes (002), (004), (101), and (104), respectively (powder diffraction file (PDF) 00-052-0875). However, it reveals the presence of Ti_2AlC (PDF 00-029-0095) with a diffraction peak at 13.0990° corresponding to the (002) plane and TiC (PDF 03-065-8805) with peaks at 36.0893° and 41.8750° corresponding to the (111) and (200) diffraction planes, respectively. Increasing the Al content to 1.2 ($Ti_3Al_{1.2}C_{1.8}$) led to a pronounced tubular-like structure (Supplementary Fig. 3c, d). This improvement is attributed to the enhanced homogeneity in the MAX phase, as higher Al content facilitates diffusion during synthesis. This ensures more consistent reactions between Ti, Al, and CF, promoting the formation of a uniform tubular structure around the CF template. The observed improvements support the critical role of controlled synthesis conditions in achieving well-defined tubular structures. While the morphology is not a perfectly round tube, it significantly improves compared to the $Ti_3Al_{1.1}C_{1.8}$ sample. The XRD pattern still shows the coexistence of Ti_2AlC, indicating an incomplete phase transformation. Still, the improved homogeneity likely aids in the gradual transformation of TiC and Ti_2AlC into Ti_3AlC_2, further supporting the development of a tubular morphology. Increasing the C content to 1.9 while maintaining Al at 1.1 ($Ti_3Al_{1.1}C_{1.9}$) resulted in a mixture of typical layered MAX phases and rod structures (Supplementary Fig. 3e, f). The XRD pattern (Supplementary Fig. 2) shows a decrease in the peak intensity at 9.7290° for the Ti_3AlC_2 MAX phase and an increase in the peak intensity for TiC at 36.1516° (111) and 41.9449° (200). This result confirms that excess carbon promotes the formation of TiC at the expense of Ti_3AlC_2. The rod-like structure is evident for the $Ti_3Al_{1.2}C_{1.9}$ MAX phase (Supplementary Fig. 3g, h), similar to the morphology observed for the $Ti_3Al_{1.1}C_{1.9}$ compound (Supplementary Fig. 3e, f).

Recognizing the advantages of tubular morphology for applications that require continuous carrier transport and a significant interface with active sites, we focused on the $Ti_3Al_{1.2}C_{1.8}$ compound, which supports the formation of these tubular structures. We hypothesized that extending the synthesis time might result in a more homogeneous and well-defined microsized tubular MAX phase. The elemental mapping of the compound $Ti_3Al_{1.2}C_{1.8}$ (Supplementary Fig. 4) confirms the presence of Ti, Al, and C, another evidence that the molar ratio of 3:1.2:1.8 (Ti: Al: C) allows obtaining a homogeneous distribution of the elements within the MAX phase. The peak observed at 2.035 keV is related to the W coating used to prepare the SEM-Energy-dispersive X-ray spectroscopy (EDS) sample. Therefore, we extended the dwell time to 10 h for that composition (Supplementary Table 1).

The XRD pattern for the $Ti_3Al_{1.2}C_{1.8}$ compound synthesized with 10-h dwell time at 1250 °C is shown in Fig. 1a. The diffraction peaks at 9.5566, 19.1404, 34.0409, and 39.0246° correspond, respectively, to the characteristic diffraction planes (002), (004), (101) and (104) of the Ti_3AlC_2 MAX phase (PDF 00-052-0875)[18]. SEM analysis revealed a more homogeneous and well-formed tubular structure (Fig. 1b, Supplementary Fig. 5) compared to the 7-hour dwell time sample (Supplementary Fig. 3c). It is also observed that in the corresponding MAX phase synthesized with a 7-hour dwell time, there is a higher presence of tiny grains that facilitate the initial formation of the tubular structure. However, with the extended 10-hour dwell time

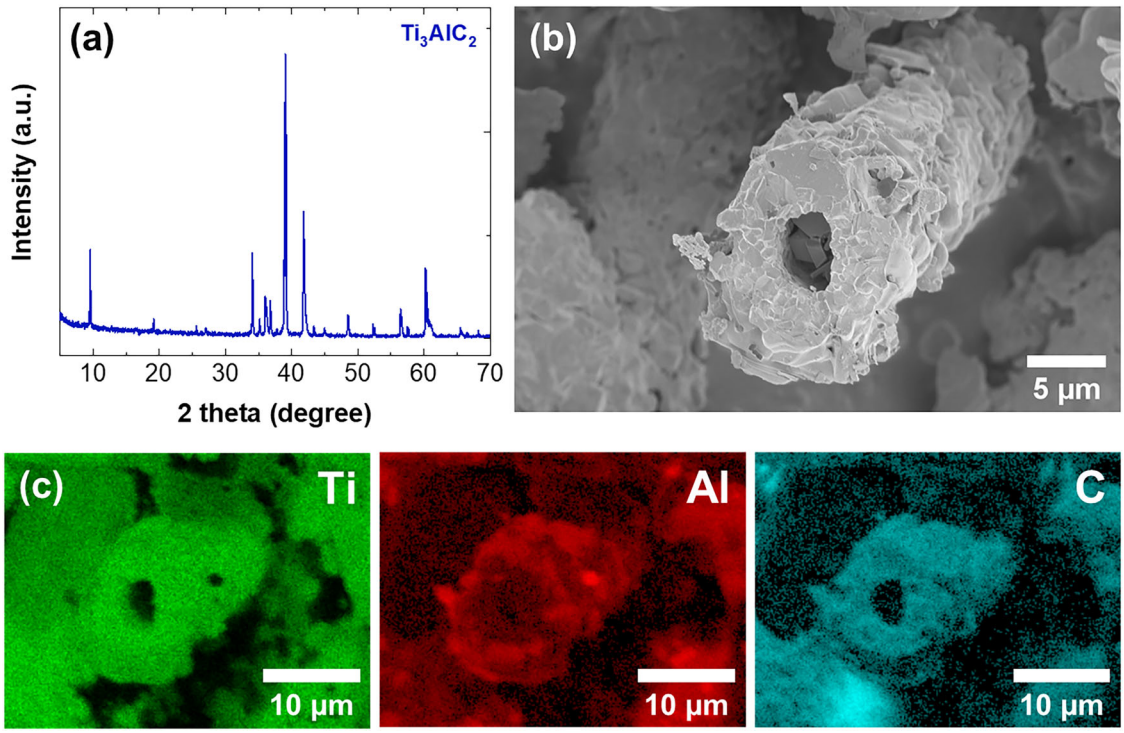

Fig. 1 | Characterization of Ti_3AlC_2 MAX phase synthesized at 1250 °C with a dwell time of 10 h by molten salts in air. a X-ray diffraction pattern; **b** scanning electron microscopy micrograph and respective, **c** elemental mapping.

(Fig. 1b), these smaller grains appear to have fused into more significant layers, likely forming a more continuous and organized layered MAX phase structure. This transformation may be attributed to the prolonged reaction time, which allows the grains to grow and coalesce, resulting in a more defined and stable tubular MAX phase. Elemental mapping (Fig. 1c) shows a uniform distribution of Ti, Al, and C elements.

These findings identified the optimal synthesis conditions to obtain a homogeneous tubular Ti_3AlC_2 MAX phase as a Ti: Al: C molar ratio of 3:1.2:1.8 with a dwell time of 10 hours at 1250 °C. Beyond the synthesis parameters, the controlled morphology of the resulting tubular-like structures is attributed to the use of CF. The carbon precursor acts as a template, as observed in other studies investigating the influence of different carbon sources used as templates for the growth of MAX phases[10–13]. For example, in the synthesis of Ti_3AlC_2 using rGO nanoflakes, it was observed that Ti_2AlC grains further react with TiC to form the final product Ti_3AlC_2[12]. In our work, the formation mechanism of a hollow structure also includes reactions between TiC and Ti_2AlC, which has been discussed previously[11]. Once KBr and Al melt, Ti particles dissolve into the MS medium as the temperature rises. The dissolved Ti and Al atoms diffuse to the CF surface, where reactions between Ti, Al, and C initiate the formation of a TiC/Ti_2AlC shell around the CF. As the reactions progress, carbon atoms from the CF diffuse outward through the TiC/Ti_2AlC shell, reacting with Ti and Al atoms on the outer surface. This diffusion process leads to the development of a hollow tubular structure. With further temperature increases, TiC and Ti_2AlC react to form Ti_3AlC_2, completing the transformation into a tubular Ti_3AlC_2 MAX phase. Our experimental results align with this mechanism. The XRD patterns of the MAX phases synthesized with a 7-hour dwell time (Supplementary Fig. 2) show the coexistence of Ti_2AlC and TiC, while the extended 10-hour dwell time facilitates their transformation into Ti_3AlC_2. SEM images (Supplementary Fig. 3) reveal that the micro-rods initially comprised several ceramic grains that formed around the CF, which acted as a template. These grains coalesce into a more continuous tubular structure with prolonged reaction time. The diffusion of Ti and Al atoms on the CF surface is facilitated by the MS medium, which forms the TiC/Ti_2AlC shell and drives the reaction toward the formation of the tubular Ti_3AlC_2 MAX phase (Fig. 1b)[11]. It is also suggested that an increased amount of Al enhances the diffusion of elements, enabling the formation of hollow microsized Ti_3AlC_2 MAX phases. Moreover, the presence of MS facilitates the ion diffusion and the formation of these tube-like geometric structures, further confirming that the MS methods enhance the reaction kinetics in the synthesis of MAX phases.

Finally, the rate-limiting step in the synthesis is primarily governed by the diffusion kinetics of Ti, Al, and CF within the MS medium and their interactions with the CF template. While the MS medium provides a liquid environment that enhances ion mobility and accelerates reaction rates, the overall synthesis remains constrained by the atomic diffusion across the TiC/Ti_2AlC shell formed on the CF surface. This diffusion process, critical for achieving the tubular morphology, highlights the correlation between synthesis parameters such as dwell time and the MS medium; thus, extending the dwell time to 10 hours significantly improved diffusion efficiency, resulting in a more homogeneous and well-defined tubular Ti_3AlC_2 MAX phase.

Beyond the tubular morphology achieved in this study, the approach of using CF as both a carbon source and template highlights the versatility of this synthesis method. Given the demonstrated role of carbon precursors in shaping MAX phases, as discussed in previous studies[10–13], our results reinforce this concept and show that CF enables the formation of a well-defined tubular morphology. These findings confirm that this methodology can be extended by selecting appropriate templates to synthesize MAX phases and MXenes with tailored morphologies, such as circular, spherical, or other shapes. Tailoring the shape and structure of the precursor can unlock new possibilities for designing MXenes with optimized properties for a wide range of applications.

Synthesis of $Ti_3C_2T_x$ MXene

With this understanding of morphology control, the next step was to selectively etch the Ti_3AlC_2 MAX phase to obtain the corresponding tubular $Ti_3C_2T_x$ MXene. This process was carried out using the MS[3] in-air method with $CuCl_2$ as the Lewis acid etchant[16,19].

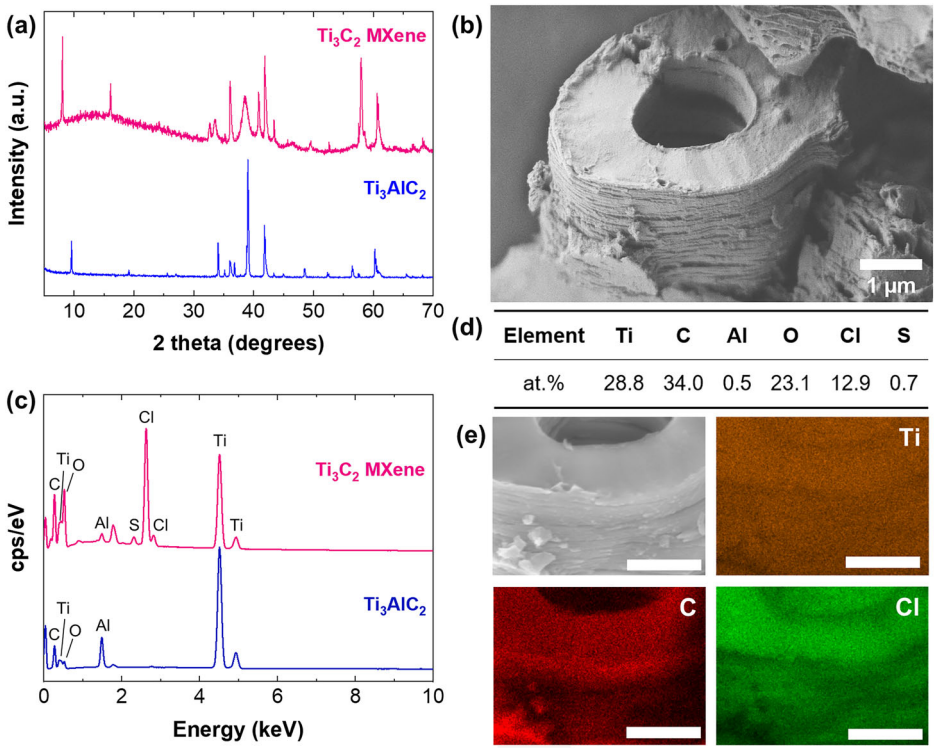

Fig. 2 | XRD and SEM-EDS characterization of tubular $Ti_3C_2T_x$ MXene synthesized at 700 °C with a dwell time of 40 minutes by molten salts in air. **a** X-ray diffraction pattern compared to the precursor MAX phase; **b** scanning electron microscopy micrograph showing tubular morphology; **c** Energy-dispersive X-ray spectroscopy (EDS) spectra compared with the precursor MAX phase; **d** elemental EDS quantification of elements (at. %) and **e** elemental mapping of elements in the MXene. The scale bar in (**e**) denotes 1 µm.

Figure 2 presents the results of the morphological and structural characterization results for the synthesized $Ti_3C_2T_x$ MXene derived from the corresponding tubular Ti_3AlC_2 MAX phase (Fig. 1), which was synthesized at 1250 °C with a dwell time of 10 h using the MS[3] method in air. The XRD patterns in Fig. 2a show a peak shift in the (002) plane from 9.5566° (Ti_3AlC_2) to 8.0421° ($Ti_3C_2T_x$) and in the (004) plane from 19.1404° (Ti_3AlC_2) to 16.0851° ($Ti_3C_2T_x$), indicating an enlarged lattice parameter. The absence of the characteristic sharp peak (104) at 39.0246 ° for the MAX phase, which is due to the presence of Al, confirms the etching of Al and the obtaining of MXene layers. These changes in the diffraction patterns confirm the etching of the MAX phase. Cubic TiC was also identified with diffractions at 36.0316 ° and 41.8392 °. The SEM image of $Ti_3C_2T_x$ MXene (Fig. 2b) reveals a well-defined 2D morphology and the tube-like geometry conferred by the CF used in the synthesis of the MAX phase. The layers of $Ti_3C_2T_x$ MXene appear large, smooth and flat, indicative of the greater surface area typically associated with 2D materials.

In contrast, the MAX phase tubes exhibit a different morphology. The SEM images of the initial MAX phases synthesized (Supplementary Fig. 3) show that these tubes are composed of grains that aggregate to form a hollow structure. This particulate assembly gives the tubes a characteristic rough and uneven surface. After extending the dwell time to 10 hours, as mentioned earlier, these smaller grains appear to have fused into more significant layers, likely forming a more continuous and organized layered MAX phase structure (Fig. 1b). Upon etching of the Al from the MAX phase, significant morphological changes occur. The etching process disrupts the tightly packed crystalline structure of Ti_3AlC_2, leading to the obtaining of MXene layers. These formed MXene layers are flat and display a coherent planar structure, unlike the rough, particle-based structure of the MAX phase hollows. This transformation can be attributed to the removal of Al, which allows the Ti and C layers to separate more easily, forming smoother and more contiguous layers. With the small particles and grains attached to the surface and the Al interlayers removed from the parent MAX phase during the etching process, the resulting tubular $Ti_3C_2T_x$ MXene appears to have smoother, cleaner and loosely packed layers. The well-defined tube-like structure of the MXene highlights the fact that the high-quality MAX phase directly influences the structural integrity and performance potential of the MXene. After etching, the tubular morphology was retained, which offers significant benefits for targeted applications. Specifically, the tubular architecture increases the accessibility of MXene layers by exposing a larger surface area, reducing diffusion distances, and enabling more efficient transport. The high specific surface area also increases the number of accessible active sites for ion and electron interactions, facilitating improved charge transfer kinetics. For instance, the hollow core can allow electrolyte infiltration in electrochemical applications, ensuring efficient mass transport to active sites and reducing concentration polarization during reactions. Beyond energy storage, the tubular morphology can facilitate rapid diffusion in gas separation and liquid filtration processes. In sensing applications, the high surface area and open geometry allow direct exposure of active sites, enhancing sensitivity and response times. Similarly, the tubular structure in catalysis could provide multiple accessible active sites and efficient reactant transport, optimizing reaction kinetics.

The EDS elemental mapping (Fig. 2c-e) confirms a homogeneous distribution of Ti and C within MXene. The presence of Cl in the EDS spectrum (Fig. 2c) results from using $CuCl_2$ as the Lewis acid, confirming the Cl as surface terminals. The homogeneous distribution of Cl in the elemental mapping (Fig. 2e) represents 12.9 wt.% (Fig. 2d). Oxygen, measured at 23.1 at.% (Fig. 2d), could arise from ammonium persulfate (APS) washing, which removes Cu and results in the addition of O-based surface groups[16]. The removal of Cu is evidenced by the absence of peaks (Fig. 2c) at typical X-ray wavelengths of Cu (Lα = 0.93 keV, Kα = 8.04 keV, and Kβ = 8.91 keV)[20]. The remaining measured Al (0.5 wt.%, Fig. 2d) can be attributed to Al atoms trapped between layers during the etching process, deposited on the surface of MXene, or originating from Al_2O_3 residues from the MAX phase[21]. The trace of S (Fig. 2c, d) is related to using APS to wash MXene and remove Cu. As for the MAX phase, the presence of W is attributed to the coating used for SEM-EDS measurements.

Additionally, to further explore the morphology and internal structure, the tubular MXene was investigated by High-Resolution Scanning Transmission Electron Microscopy (HRSTEM) (Fig. 3). The lift-out procedure was targeted right to the middle of the microtube, allowing visualization of its cross-section. Therefore, the measurement provided a visualization of two columns with spacing in between corresponding to the tube cavity

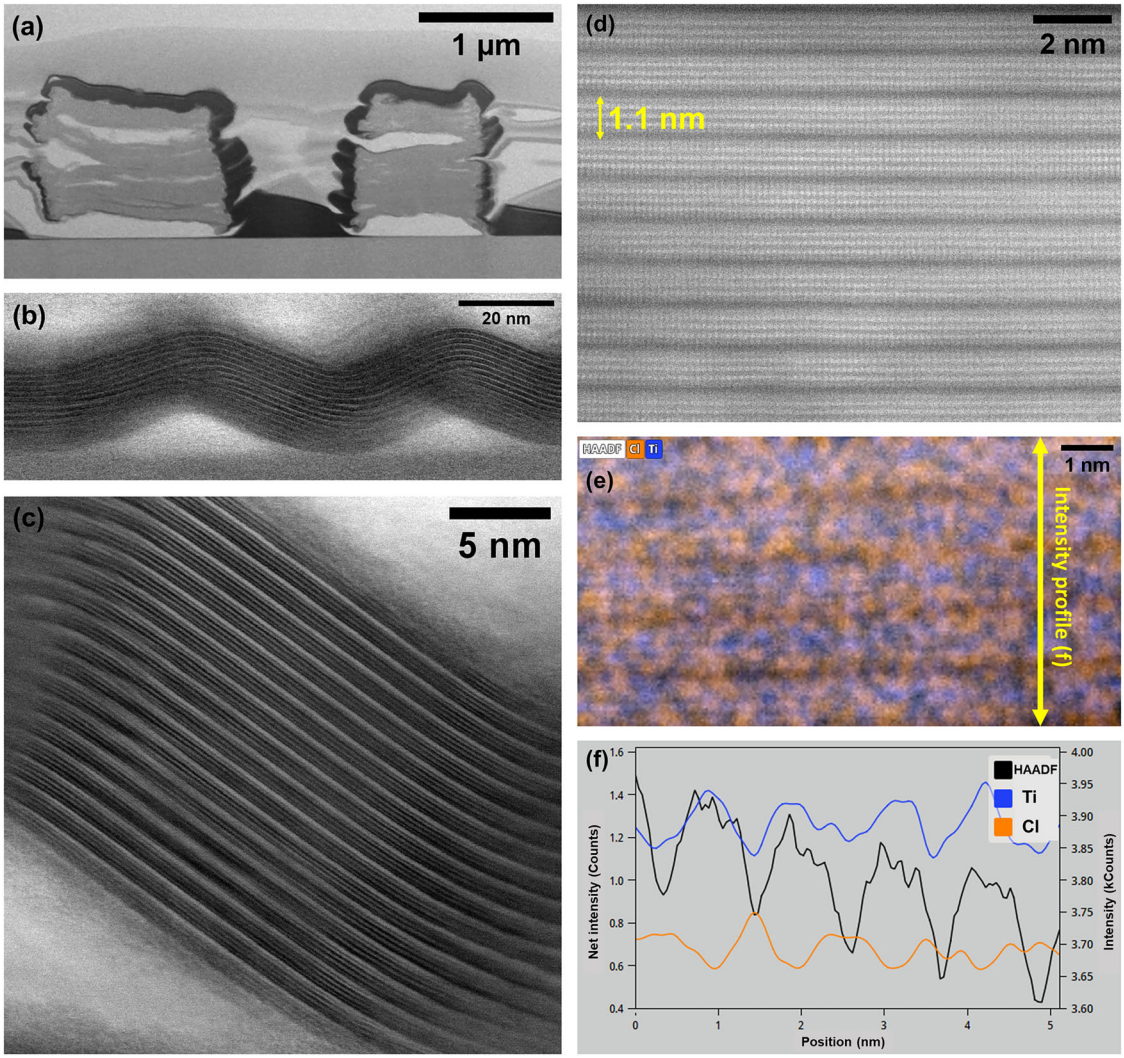

Fig. 3 | Transmission electron microscopy analysis of the cross-section of tubular $Ti_3C_2T_x$ MXene. a Low magnification scanning Transmission Electron Microscopy-High Angle Annular Dark-Field (TEM-HAADF) image showing the tube cross-section, with two columns representing the MXene structure and the central space indicating the tube cavity; **b** TEM bright-field image displaying the MXene layers in the cross-section, and **c** its detailed image; **d** High-Resolution Scanning Transmission Electron Microscopy (HRSTEM)-HAADF image of the MXene cross-section, showing the interlayer spacing; **e** HRSTEM-Energy-dispersive X-ray spectroscopy elemental mapping of Ti and Cl within the structure, and respective **f** periodicity of the HAADF signal profile corresponding to the distribution of Ti and Cl across the layers. The yellow arrow in **e** corresponds to the signal profile.

(Fig. 3a), emphasizing the hollow tubular morphology maintained after etching. The layered structure with several macroscopic cavities between layers is evident from the low-magnification image (Fig. 3a).

Figure 3b and Fig. 3c present the TEM bright-field imaging of the MXene layers in the cross-section, revealing the formation of wrinkles and providing a detailed look at the layered structure. A close-up of these layers (Fig. 3c) further illustrates the well-defined interlayer arrangement.

A detailed HRSTEM-High-Angle Annular Dark-Field (HAADF) image of the MXene tube segment (Fig.3b-d) offers an in-depth view of the layered structure, showing the formation of wrinkles (Fig. 3b) and revealing an interlayer spacing of 1.1 nm between layers (Fig. 3d). The corresponding elemental mapping (Fig. 3e) and intensity profiling (Fig. 3f) further elucidate the distribution of elements within the structure. The HAADF signal, which is sensitive to atomic number, aligns closely with the positions of titanium (Ti) atoms, confirming the periodic arrangement of Ti layers. The chlorine atom (Cl) signal is prominently located on the edges of the individual layers, supporting the existence of -Cl terminations on the MXene surface. This is a direct result of the etching process using $CuCl_2$, which facilitates the introduction of Cl surface terminations.

The retention of the tube-shaped morphology and the distribution of elements observed in HRSTEM are other evidence of the successful synthesis of tubular $Ti_3C_2T_x$ MXene. The careful synthesis conditions, including the use of CF as a template and the MS[3] method in air, contribute to creating this unique structure, which combines the advantageous properties of MXenes with the potential structural benefits conferred by the tubular shape.

The surface chemistry of the tubular MXene was further investigated in greater detail by X-ray photoelectron spectroscopy (XPS), Supplementary Fig. 6-9. First, the precursor MAX phase was analyzed. Initial XPS analysis revealed the presence of a thick layer of adsorbed species such as hydrocarbons, CO_2, or H_2O on its surface, which hindered the signal from other elements (Supplementary Fig. 6a). Ar sputtering was performed to remove these adsorbates. Subsequently, nitrogen appeared in the survey spectrum (Supplementary Fig. 6b), likely originating from the residual atmosphere. A comparison of the survey spectra from all processing steps (Supplementary Fig. 6), including the analysis before (Supplementary Fig. 6c) and after (Supplementary Fig. 6d) the APS washing step, highlights the transformation in surface chemistry from the MAX phase to the tubular MXene, emphasizing the changes in elemental composition. During the etching

process, copper (Cu) was adsorbed on the surface of MXene (Supplementary Fig. 6c, Supplementary Fig. 8f) due to the use of $CuCl_2$. However, APS treatment effectively removed Cu from the $Ti_3C_2T_x$ MXene (Supplementary Fig. 6d). The trace amount of S observed in the $Ti_3C_2T_x$ MXene survey spectrum (Supplementary Fig. 6d) is attributed to the APS washing process, which effectively removed Cu, as indicated by both EDS (Fig. 2c) and the absence of Cu peaks in the survey and HR spectrum (Supplementary Fig. 6d, S9f).

The survey spectra (Supplementary Fig. 6) also confirm the presence of aluminum in all samples; however, its concentration is significantly lower in the $Ti_3C_2T_x$ MXene samples (Supplementary Fig. 6c, d) compared to the initial MAX phase (Supplementary Fig. 6b). This reduction indicates successful exfoliation, as most aluminum is removed during etching, consistent with the EDS analysis (Fig. 2c, d). The remaining aluminum in the MXene samples is likely present as adsorbed species on the surface. Additionally, the HR Al 2p spectra (Supplementary Figs. 7b, 8c and 9c) reveal that all detected aluminum is in the form of Al_2O_3, which contributes to the higher oxygen concentration in the $Ti_3C_2T_x$ MXene.

The survey spectrum of $Ti_3C_2T_x$ MXene (Supplementary Fig. 6d) confirmed the presence of Cl with peaks at 200.6 and 199.0 eV (Supplementary Fig. 9d), confirming the presence of Ti–Cl bonds[15]. These surface terminations align with the elemental mapping results by EDS (Fig. 2c-e) and HRSTEM-HAADF analysis (Fig. 3e), indicating the successful introduction of Cl groups during the etching process.

The HR Ti 2p and C 1 s spectra of the tubular MAX phase and MXene (before and after the APS washing step) were deconvoluted into several binding states (Supplementary Fig. 7-9). In XPS of Ti, the binding energies of individual bonding states can vary slightly between different samples. Depending on the surrounding matrix and the degree of oxidation, more oxidized regions, such as TiO_2 or suboxides, can exhibit different charging behaviors compared to bare MXene. These variations in surface charging can shift the binding energy positions, leading to slight differences in peak positions between samples. Differences in defects, stoichiometry, and surface contamination can further influence these energy shifts. Spin-orbit splitting for Ti also varies between binding states, typically around 6.0–6.1 eV for metallic Ti and 5.7–5.8 eV for TiO_2[22]. In the Ti 2p spectrum of the $Ti_3C_2T_x$ MXene after APS washing (Supplementary Fig. 9a), the peaks at 454.7, 456.5, and 458.5 eV correspond to the $2p_{3/2}$ spin-orbit component of the Ti–C (I), Ti–C (II) and Ti–C (III) bonding states, representing titanium with different amount of terminals[15]. Ti–C (I) represents pure MXene in the middle of individual layers, and Ti–C (II) and Ti–C (III) represent titanium with terminals located on the basal planes and edges/defects, respectively. The peaks at 460.4, 462.2, and 464.2 eV are also assigned to the $2p_{1/2}$ component Ti–C (I-III) bonding states[15]. The 460.4 and 465.9 eV peaks originate from TiO_2[23], usually formed at edges or defect sites. The C 1 s spectrum (Supplementary Fig. 9b) displayed peaks at 282.9, 284.5, 285.5, 286.6, 287.8, and 289.5 eV corresponding to the carbide (C–Ti), and adsorbed species containing various bonding states (C–C, C = C, C–O, C = O, and O–C = O), respectively. Supplementary Table 2 summarizes Ti 2p and C 1 s spectra fitting, offering insights into the chemical transformations occurring during the etching and after APS washing. From the data, it is evident that oxidation occurs during both the synthesis and washing processes. This is indicated by the increased presence of higher oxidation states in the Ti 2p spectra. The HR spectra of O 1 s for MAX phase and MXene samples are shown in Supplementary Fig. 7d, 8 d, and 9 d. The O 1 s spectrum suggests the presence of –O terminals in the $Ti_3C_2T_x$ MXene (Supplementary Fig. 9d), but it is important to note that oxygen contributions can arise from multiple sources. $Ti_3C_2T_x$ MXenes are sensitive to oxidation[24], and surface O-terminations commonly form during synthesis. Additionally, washing steps after the synthesis process, specifically in this work with APS, can contribute to the replacement of Cl terminations by oxygen-containing functional groups[15,25]. Furthermore, the presence of Al_2O_3, as confirmed by the Al 2p spectrum, likely contributes to the O 1 s signal, further highlighting the complex nature of surface chemistry in MXenes.

Building on these structural and chemical insights, we performed initial electrochemical measurements to demonstrate the potential of the synthesized tubular $Ti_3C_2T_x$ MXene. Although this work primarily focuses on synthesizing and comprehensively characterizing these unique tubular MXene architectures, preliminary electrochemical testing provides insight into their performance as anode materials in lithium-ion batteries. Key metrics, including charge-discharge profiles, differential capacity (dQ/dV) plots, cycling stability, and rate performance, were analyzed to assess the behavior and initial performance of the tubular MXene (Fig. 4).

Figure 4a illustrates multiple voltage plateaus during discharge, with an initial discharge capacity of 500.1 mAh g^{-1}, corresponding to the lithiation process. This behavior suggests significant structural or phase changes in the material during initial cycling. The plateau around 0.75 V is associated with electrolyte interphase (SEI) formation, a common phenomenon in lithium-ion battery systems. The dQ/dV analysis in Fig. 4b shows multiple lithiation peaks, which may be associated with the complex structural components of the MXene. As confirmed by EDS (Fig. 2c, d), TEM (Fig. 3e), and XPS (Supplementary Fig. 6d, Supplementary Fig. 9e), the MXene contains –Cl terminations, and together with –O surface terminations (Fig. 2c, d, and Supplementary Fig. 9d), leading to different electrochemical processes during lithiation. However, during the delithiation (charging) process, only a reversible capacity of 157.9 mAh is observed, with no evident oxidation plateau or delithiation dQ/dV peaks, indicating irreversible phase transitions and capacity loss during the initial cycle, consistent with findings reported in the literature[26–28]. The formation of electrochemically inert compounds such as LiCl and Li_2O, resulting from the interaction of Li with the surface components, likely contributes to this behavior, along with SEI formation. The absence of prominent redox peaks in subsequent cycles indicates that capacitive behavior predominantly contributes to the capacity in later cycles. The O-based surface terminations, in particular, may provide stable sites for ion adsorption, influencing the capacitive contributions in subsequent cycles. The role of O-terminations in improving Li-ion capacity has been reported in previous studies[29], where lithiated O-terminated MXenes exhibited a strong interaction between O and Li, leading to enhanced capacity. Given the oxygen content in our tubular MXene (Fig. 2c, d, and Supplementary Fig. 9d), a similar effect could contribute to the electrochemical performance observed in this work.

The cycling stability of the MXene anode at 50 mAh g^{-1}, presented in Fig. 4c, shows a gradual decrease (0.2% per cycle) in capacity over 200 cycles, with an initial capacity of 97.7 mAh^{-1}. However, it can be said that the tubular structure enhances the MXene's ability to retain a significant portion of its capacity over cycling. Furthermore, the rate performance (Fig. 4d) highlights the role of the tubular morphology in facilitating rapid ion transport. At various current densities (10, 20, 50, 100, and 200 mA g^{-1}), the MXene demonstrates 158, 105, 84, 68, and 63 mAh g^{-1} capacities. The observed moderate capacity decrease as the current density increases is typical for many anode materials, and it is attributed to kinetic limitations and polarization effects at higher rates. However, the tubular structure likely contributes to the ability of MXene to retain a significant portion of its capacity at higher current densities, primarily by providing a larger surface area and shorter ion diffusion paths. This structure facilitates faster and more efficient lithium-ion transport during charge and discharge cycles, reducing the likelihood of kinetic limitations and polarization effects, which typically occur at higher rates.

Consequently, enhanced ion accessibility and reduced diffusion distances help maintain higher capacity even as the current density increases, which is crucial for high-power applications. With these initial electrochemical data, the study laid the groundwork for future investigations in optimizing the performance of tubular MXenes. It encourages further exploration of different synthesis parameters, modifications, and potential applications in various energy storage technologies.

Conclusions

Here, we present the synthesis of the Ti_3AlC_2 MAX phase using carbon microfibers (CF) as a carbon source and template to achieve tubular

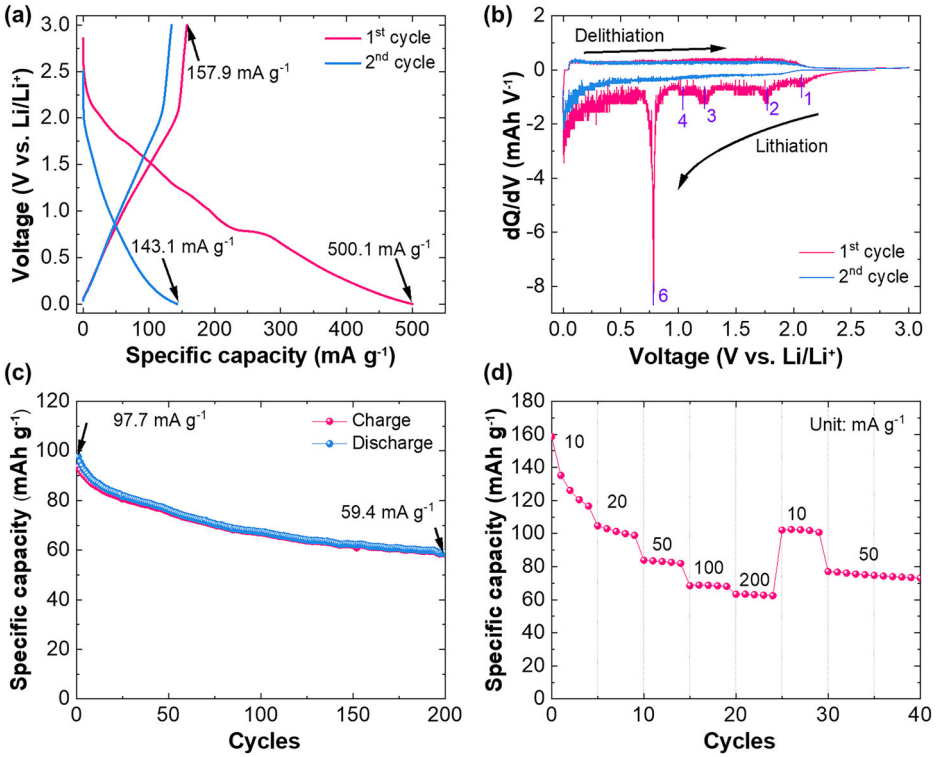

Fig. 4 | Electrochemical performance of tubular $Ti_3C_2T_x$ MXene as an anode in lithium-ion batteries. a Initial charge and discharge voltage profiles at 10 mAh g^{-1} and **b** corresponding differential capacity (dQ/dV) curves; **c** Cycling stability at 50 mAh g^{-1} after initial cycling; **d** Rate performance at different current densities.

morphology. The corresponding $Ti_3C_2T_x$ MXene was then synthesized from this MAX phase, retaining its tubular structure and thus representing a significant achievement in the synthesis of MXenes. Both processes were carried out using the molten salts shielded method in air. $CuCl_2$, as a Lewis acid, enabled the etching of the MAX phase, thus obtaining $Ti_3C_2T_x$ MXene rich in Cl terminations. Morphological and structural characterization confirmed the MAX phase and MXene synthesis with a well-preserved tubular architecture. Electrochemical testing demonstrated the potential of this tubular MXene as a high-performance anode in lithium-ion batteries, with significant capacity retention at higher current densities. Shaping the morphology of MXenes, as achieved here with tubular structures, is crucial for optimizing their properties, including improving ion diffusion and maximizing surface area, which is critical for energy storage applications. CF not only opens new possibilities for tailoring the properties of MXenes and their precursors but also expands their functionality across different applications, such as gas sensing, liquid filtration, and other technologies requiring fast diffusion processes. Future research can further explore other carbon sources and synthesis conditions to expand the MXene material family and its precursors with different morphologies and unlock their full potential across various technologies.

Methods

Synthesis of Ti_3AlC_2 MAX phase

Elemental powders of titanium (Ti), aluminum (Al), and carbon microfibers (CF) were used as precursors. The Ti (ThermoScientific, Germany, >99.5% pure, -325 mesh), Al (ThermoScientific, Germany, >99.5% pure, -325 mesh), and CF (Tenax™-A HT M100 100mu fibers, Teijin Carbon Europe GMBH, Germany, fiber length 100 µm, ⌀ 7.0 µm) were mixed in different molar ratios. All synthesis conditions are summarized in Table S1. Potassium bromide (KBr, ThermoScientific, Germany, >99% pure) was added in a 1:1 wt.% ratio. The mixture was ball-milled for 24 hours with yttria-stabilized zirconia balls (⌀ 4.8-5.2 mm) in ethanol, followed by an additional hour of mixing using a multi-directional mixer (Turbula WAB, Switzerland). The slurry was dried overnight at 60 °C, then pelletized under 70 kN pressure in a steel mold (⌀ 30 mm) using a hydraulic press (Paul-Otto Weber, Germany). The pellet was placed in an alumina crucible, shielded with KBr, and synthesized by ramping the temperature at 2 °C/min to 1250 °C, with holding times of 7 or 10 hours, and cooled at the same rate in ambient air. Post-synthesis, the KBr was dissolved with hot deionized water, and the specimen was ground to a fine slurry, washed, vacuum-filtered, dried overnight at 60 °C, and sieved through a 106 µm mesh using a Vibratory Sieve Shaker AS 200 Basic (Retsch Technology, Germany). This process yielded the final Ti_3AlC_2 MAX phase powder.

Synthesis of MXene

The synthesis of MXene is based on a previously reported procedure[19]. Briefly, 0.5 g of Ti_3AlC_2 MAX phase powder is mixed with a eutectic salt (NaCl: KCl in a 1:1 molar ratio; NaCl and KCl from ThermoScientific, Germany, >99% pure) in a 1:4–6 weight ratio. The mixed powder was pelletized under 70 kN pressure using a steel mold (⌀ 20 mm) in a hydraulic press (Paul-Otto Weber, Germany). The resulting pellet was placed in a cylindrical alumina crucible (30 mL), covered with a salt mixture of 8.766 g of NaCl, 11.183 g of KCl, and 2.073 g of $CuCl_2$ ($CuCl_2$ dehydrate, from ThermoScientific, Germany, >99% pure) milled for 10 min. The crucible was covered with an alumina lid, heated to 700 °C at 10 °C/min, held for 40 minutes, and then cooled to room temperature. The material was repeatedly washed with deionized water to remove the salts and treated with 100 mL of 0.5 M ammonium peroxydisulfate (APS) (ThermoScientific, Germany) solution for 1 h at room temperature to remove Cu. Finally, the MXene was dried overnight at 35 °C and collected for further investigation.

All chemicals and materials were used as received.

Materials characterizations

X-ray diffraction (XRD) patterns were acquired using a Bruker D8 Advance instrument (Bruker AXS GmbH). The instrument was configured in Bragg–Brentano parafocusing geometry and employed a CuKα radiation source with $\lambda = 0.15418$ nm, operating at $U = 30$ kV and $I = 10$ mA. The XRD patterns were collected at room temperature, covering 2θ values from 5 to 70°, with a step size of 0.02°. Data analysis was conducted using the HighScore Plus 4.9 software package. The morphology of the MAX phase and MXene was observed by scanning electron microscopy (SEM) with a GeminiSEM 500 microscope from Zeiss (Germany) at a 1 kV acceleration

voltage. An Energy-dispersive X-ray spectroscopy (EDS) detector from Oxford Instruments was used for element analysis and operated at 10 kV acceleration voltage. Powder samples were drop-cast on carbon tape and coated with tungsten (4 nm layer thickness). A Thermo Fisher Helios 5 FX microscope was used to prepare the cross-sectional transmission electron microscopy (TEM) lamella. The TEM-preselected microtube was localized on a silicon wafer. Thick tungsten electron beam deposition was used to provide the initial protection layer to avoid beam damage caused by the gallium ions. Tungsten was chosen for its contrast in the TEM. Amorphous carbon was selected for the final ion-beam-deposited protection layer. The lamella was lifted out using a micromanipulator and subsequently transferred to a copper focused ion beam (FIB) grid. The thinning and polishing procedure was performed with FIB accelerating voltages ranging from 30 kV to 2 kV and beam currents ranging from 2 nA to 26 pA. The TEM analysis was executed on a double aberration-corrected Themis-Z microscope (Thermo Fisher Scientific Electron Microscopy Solutions, Hillsboro, USA) at an accelerating voltage of 200 kV. HR-XPS was performed using a SPECS spectrometer (Specs, Germany) equipped with a monochromatic Al Kα X-ray radiation source (1486.7 eV) and a hemispherical electron analyzer Phoibos 150. The samples were placed on a conductive carbon tape and compensated with a flood gun to yield a C 1 *s* peak at 285 eV. The survey spectra were recorded with E_p set to 100 eV, and the core lines' high-resolution (HR) spectra with E_p set to 20 eV. HR scans were performed for C 1 s, O 1 s, Ti 2p, Al 2p, Cl 2p and Cu 2p core levels. The base chamber pressure during the acquisitions was 10^{-9} mbar or lower. Due to a heavy charge development on the samples' surface, a low-energy electron flow generated by an electron flood gun has been used to compensate for the charge buildup. The Casa XPS software package was used for quantification and curve-fitting on the core-level spectra using Shirley-type backgrounds.

Electrochemical characterization

The Li-ion storage capabilities were assessed using standard CR-2032 coin-type half cells sourced from Neware (China). A pre-mixed slurry was prepared to fabricate the working electrodes, comprising 80 wt.% of the synthesized MXene, 10 wt.% of carbon black, and 10 wt.% of polyvinylidene fluoride. This slurry was then applied onto nickel foam and pressed into thin sheets. Lithium foil served as the counter and reference electrode, while a polypropylene film (Celgard 2400) was used as the separator. The electrolyte used was a solution of 1 M $LiPF_6$ dissolved in a mixture of ethylene carbonate, dimethyl carbonate, and diethyl carbonate in a 1:1:1 volume ratio. All electrochemical performance tests were carried out at room temperature using a Neware battery testing system (BTX 8.0, Shenzhen, China).

Data availability

The datasets generated and/or analyzed during the current study are accessible via the Zenodo repository: https://doi.org/10.5281/zenodo.14882040.

Received: 18 November 2024; Accepted: 18 March 2025;
Published online: 26 March 2025

References

1. Naguib, M. et al. Two-dimensional nanocrystals produced by exfoliation of Ti_3AlC_2. *Adv. Mater.* **23**, 4248–4253 (2011).
2. Deysher, G. et al. Synthesis of Mo_4VAlC_4 MAX phase and two-dimensional Mo_4VC_4 MXene with five atomic layers of transition metals. *ACS Nano* **14**, 204–217 (2020).
3. Wyatt, B. C., Rosenkranz, A. & Anasori, B. 2D MXenes: tunable mechanical and tribological properties. *Adv. Mater.* **33**, 2007973 (2021).
4. Gonzalez-Julian, J. Processing of MAX phases: From synthesis to applications. *J. Am. Ceram. Soc.* **104**, 659–690 (2021).
5. Vahidmohammadi, A., Rosen, J. & Gogotsi, Y. The world of two-dimensional carbides and nitrides (MXenes). *Science* **372**, eabf1581 (2021).
6. Bhat, A. et al. Prospects challenges and stability of 2D MXenes for clean energy conversion and storage applications. *NPJ 2D Mater. Appl* **5**, 61 (2021).
7. Bai, X. & Guan, J. Applications of MXene-based single-atom catalysts. *Small Struct.* **4**, 2200354 (2023).
8. Oliveira, F. M., Azadmanjiri, J., Wang, X., Yu, M. & Sofer, Z. Structure design and processing strategies of MXene-based materials for electromagnetic interference shielding. *Small Methods* **7**, 2300112 (2023).
9. Ho, D. H., Choi, Y. Y., Jo, S. B., Myoung, J.-M. & Cho, J. H. Sensing with MXenes: progress and prospects. *Adv. Mater.* **33**, 2005846 (2021).
10. Yang, L. X., Wang, Y., Zhang, H. L., Liu, H. J. & Zeng, C. L. A simple method for the synthesis of nanosized Ti_3AlC_2 powder in NaCl–KCl molten salt. *Mater. Res Lett.* **7**, 361–367 (2019).
11. Liu, Y. et al. Facile synthesis of hollow Ti_3AlC_2 microrods in molten salts via Kirkendall effect. *J. Adv. Ceram.* **11**, 1491–1497 (2022).
12. Shao, H. et al. Synthesis of MAX phase nanofibers and nanoflakes and the resulting MXenes. *Adv. Sci.* **10**, 2205509 (2023).
13. Siebert, J. P., Flores, M. & Birkel, C. S. Shape control of MAX phases by biopolymer sol−gel synthesis: Cr_2GaC thick films, microspheres, and hollow microspheres. *ACS Org. Inorg. Au* **2021**, 59–65 (2022).
14. Dash, A., Vaßen, R., Guillon, O. & Gonzalez-Julian, J. Molten salt shielded synthesis of oxidation prone materials in air. *Nat. Mater.* **18**, 465–470 (2019).
15. Li, M. et al. Element replacement approach by reaction with lewis acidic molten salts to synthesize nanolaminated MAX phases and MXenes. *J. Am. Chem. Soc.* **141**, 4730–4737 (2019).
16. Li, Y. et al. A general Lewis acidic etching route for preparing MXenes with enhanced electrochemical performance in non-aqueous electrolyte. *Nat. Mater.* **19**, 894–899 (2020).
17. Gao, L. et al. Preparation and performance of MAX phase Ti_3AlC_2 by in-situ reaction of Ti-Al-C system. *Adv. Powder Technol.* **31**, 3533–3539 (2020).
18. Tzenov, N. V. & Barsoum, M. W. Synthesis and characterization of Ti_3AlC_2. *J. Am. Ceram. Soc.* **83**, 825–832 (2000).
19. Chen, J. et al. Molten salt-shielded synthesis (MS^3) of MXenes in Air. *Energy Environ. Mater.* **6**, e12328 (2021).
20. Bearden, J. A. X-Ray wavelengths. *Rev. Mod. Phys.* **39**, 78–124 (1967).
21. Näslund, L.-Å., Persson, P. O. Å. & Rosen, J. X-ray photoelectron spectroscopy of Ti_3AlC_2, $Ti_3C_2T_z$, and TiC provides evidence for the electrostatic interaction between laminated layers in MAX-Phase Materials. *J. Phys. Chem. C.* **124**, 27732–27742 (2020).
22. Biesinger, M. C., Lau, L. W. M., Gerson, A. R. & Smart, R. S. Resolving surface chemical states in XPS analysis of first row transition metals, oxides and hydroxides: Sc, Ti, V, Cu and Zn. *Appl Surf. Sci.* **257**, 887–898 (2010).
23. Han, M. et al. Ti_3C_2 MXenes with modified surface for high-performance electromagnetic absorption and shielding in the X-band. *ACS Appl Mater. Interfaces* **8**, 21011–21019 (2016).
24. Habib, T. et al. Oxidation stability of $Ti_3C_2T_x$ MXene nanosheets in solvents and composite films. *NPJ 2D Mater. Appl* **3**, 8 (2019).
25. Su, T. et al. Surface engineering of MXenes for energy and environmental applications. *J. Mater. Chem. A* **10**, 10265–10296 (2022).
26. He, Y. et al. Self-assemble and in-situ formation of laponite RDS-decorated d-$Ti_3C_2T_x$ hybrids for application in lithium-ion battery. *ChemistrySelect* **4**, 10694–10700 (2019).
27. Xu, M. et al. Opening magnesium storage capability of two-dimensional MXene by intercalation of cationic surfactant. *ACS Nano* **12**, 3733–3740 (2018).
28. Guo, Z. et al. Sulfur-decorated Ti3C2Tx MXene for high-performance sodium/potassium-ion batteries. *Chem. Asian J.* **18**, e202300336 (2023).
29. Xie, Y. et al. Role of surface structure on li-ion energy storage capacity of two-dimensional transition-metal carbides. *J. Am. Chem. Soc.* **136**, 6385–6394 (2014).

Acknowledgements
The authors acknowledge the assistance provided by the Advanced Multiscale Materials for Key Enabling Technologies project, supported by the Ministry of Education, Youth and Sports (MEYS), Project No. CZ.02.01.01/00/22_008/0004558, Co-funded by the European Union. FMO was supported by the Johannes Amos Comenius Programme, the European Structural and Investment Funds, with CHEMFELLS V (project no. CZ.02.01.01/00/22_010/0003004) from the MEYS. The authors acknowledge Prof. Reshef Tenne from the Weizmann Institute of Science for funding the tool time on the Themis-Z microscope. Z.S. was supported by Czech Science Foundation (GACR No. 23-05918S). This work was supported by project Know4Nano (grant agreement Nr. 101159710) and by the European Union's Horizon Europe research and innovation programme under grant agreement ID 101135196.

Author contributions
F.M.O., conceptualization, data curation, validation, formal analysis, investigation, visualization, writing—original draft, writing—review and editing. B.W., formal analysis, validation, investigation, writing—review and editing. V.M., formal analysis, validation, investigation, writing—review and editing. V.K., data curation, validation, writing—review and editing. K.B., investigation, writing—review and editing. L.H., investigation. Z.S., conceptualization, supervision, validation, project administration, funding acquisition, writing—review and editing. J.G.J., conceptualization, supervision, validation, writing—review and editing. All the authors contributed to the manuscript.

Competing interests
The authors declare no competing interests.

Additional information
Supplementary information The online version contains supplementary material available at https://doi.org/10.1038/s43246-025-00786-3.

Correspondence and requests for materials should be addressed to Filipa M. Oliveira, Zdeněk. Sofer or Jesus Gonzalez-Julian.

Peer review information *Communications Materials* thanks Qing Huang and the other, anonymous, reviewer(s) for their contribution to the peer review of this work. Primary Handling Editors: Mengqiang Zhao and John Plummer. A peer review file is available.

Reprints and permissions information is available at http://www.nature.com/reprints

Publisher's note Springer Nature remains neutral with regard to jurisdictional claims in published maps and institutional affiliations.

Open Access This article is licensed under a Creative Commons Attribution-NonCommercial-NoDerivatives 4.0 International License, which permits any non-commercial use, sharing, distribution and reproduction in any medium or format, as long as you give appropriate credit to the original author(s) and the source, provide a link to the Creative Commons licence, and indicate if you modified the licensed material. You do not have permission under this licence to share adapted material derived from this article or parts of it. The images or other third party material in this article are included in the article's Creative Commons licence, unless indicated otherwise in a credit line to the material. If material is not included in the article's Creative Commons licence and your intended use is not permitted by statutory regulation or exceeds the permitted use, you will need to obtain permission directly from the copyright holder. To view a copy of this licence, visit http://creativecommons.org/licenses/by-nc-nd/4.0/.

© The Author(s) 2025